Available online at www.sciencedirect.com
ScienceDirect
International Journal of Heat and Fluid Flow 27 (2006) 911–923
International Journal of HEAT AND FLUID FLOW
www.elsevier.com/locate/ijhff

LES of a free annular swirling jet – Dependence of coherent structures on a pilot jet and the level of swirl

Manuel García-Villalba *, Jochen Fröhlich

SFB 606, University of Karlsruhe, Kaiserstr. 12, 76128, Karlsruhe, Germany

Received 23 September 2005; received in revised form 29 January 2006; accepted 4 March 2006
Available online 15 June 2006

Abstract

The paper presents large eddy simulation of unconfined swirling jets. In the first part, an unconfined annular jet is investigated for swirl numbers ranging from 0 to 1.2. The impact of the swirl on the mean flow and the precessing vortex structures in this flow is analysed. In the second part of the paper, a co-annular pilot jet is introduced near the axis. The investigations show that the additional swirl near the axis has a stronger effect than the pilot jet itself, leading to an almost entire removal of coherent structures.

Keywords: Swirling jets; Annular jets; Large eddy simulation; Coherent structures; Pilot jet

1. Introduction

Swirling flows are widely used in many engineering applications. In combustion devices, they are often employed to stabilize the flame by means of a recirculation zone. This is advantageous since it does not involve solid boundaries thus avoiding related problems of heat load on the structure. Swirling flows on the other hand are prone to instabilities leading to strong large-scale coherent structures. These influence mixing and reaction and can trigger pronounced unsteadiness of combustion possibly degrading the performance of the whole system. Lean premixed burners in modern gas turbines often contain an additional pilot jet with richer mixture, typically introduced near the axis of the swirl burner. This raises the question of how the additional jet modifies the fluid mechanical behaviour of the system and in particular the occurrence of coherent structures.

Swirling flows are difficult to model with Reynolds-averaged methods (Jakirlić et al., 2002) due to the effects of mean flow streamline curvature. The large eddy simulation (LES) approach is exempt of this problem, at the price of higher computational cost, by directly resolving the major part of the turbulent motion. LES of such flows, however is still scarce. Pierce and Moin (1998a) were among the first to perform LES of a swirl flow in a pipe with a sudden expansion. They employed a finite volume method on a staggered grid using cylindrical coordinates and obtained good results for the mean velocity and the mixture fraction of a passive scalar. Wang et al. (2004), for a similar confined configuration studied the influence of the level of swirl on the mean flow and turbulent fluctuations. Lu et al. (2005) also performed LES of a turbulent round jet issuing into a dump combustor and analysed the interaction of coherent structures with acoustic modes of the combustor. Wegner et al. (2004) performed LES of a free annular swirling jet including the swirl generating device in the computational domain and were able to detect a flow instability leading to the occurrence of large-scale coherent structures. The role of the pilot jet in cold swirling flows was also studied experimentally by Merkle et al. (2002) using a dump combustor geometry and two setups only differing by the sense of rotation of the pilot jet. It was found that the counter-rotating pilot jet considerably reduced the length of the recirculation zone and the momentum exchange perpendicular to the main flow direction.

* Corresponding author.
E-mail address: villalba@ifh.uka.de (M. García-Villalba).

0142-727X/$ - see front matter © 2006 Elsevier Inc. All rights reserved.
doi:10.1016/j.ijheatfluidflow.2006.03.015

In the present paper LES is used to study annular and co-annular jets in a prototype system corresponding to an experimental setup. Different from many other studies the jet issues into the ambient, without surrounding walls. The analysis of the results focuses on the strength and sensitivity of flow instabilities generating large-scale coherent structures. In García-Villalba et al. (2004a, 2006) the present authors performed LES of an unconfined annular swirling jet and validated the simulation method by means of detailed comparisons with experiments for the same configuration. Large scale coherent helical structures precessing around the symmetry axis at a constant rate were identified in these computations. The first goal of the present paper is to investigate the influence of the swirl parameter on these structures. Second, the impact of an additional co-annular pilot jet near the axis is studied.

2. Numerical method

The simulations have been performed with the code LESOCC2 (Hinterberger, 2004), which is a successor of the code LESOCC (Breuer and Rodi, 1996). It solves the incompressible Navier–Stokes equations on curvilinear block-structured grids. A collocated finite-volume discretization with second-order central schemes for convection and diffusion terms is employed. Temporal discretization is performed with a three-stage Runge–Kutta scheme solving the pressure-correction equation in the last stage only.

The computations for the two issues addressed in this paper have been performed with two very similar configurations. These match two experiments performed with LDA in air flow by Büchner and Petsch (2004) and by Bender and Büchner (2005) which are used for validation. The first configuration had also been investigated previously by Hillemanns (1988). For each sensitivity study one of the computations corresponds to an experiment so that these data can be used for validation. The variation of the swirl number was investigated using the geometry shown in Fig. 1 with an inner diameter of the annular jet of $0.5D$ where D is the outer diameter of the jet. The outer radius of the jet $R = D/2$ is used as the reference length in this paper. The geometry of the second configuration only differs with respect to the inlet and is detailed below. The rest of the computational domain is the same (Fig. 1). The block-structured mesh consists of about 2.5 million cells in both cases. The grid is stretched in both the axial and the radial direction to allow for concentration of points close to the jet exit and the inlet duct walls, while 100 grid points are used in the azimuthal direction. The stretching factor is everywhere less than 5%. The minimum axial spacing appears at the jet outlet and is $\Delta x = 0.02R$. Close to the walls, the minimum radial spacing is $\Delta r = 0.012R$. In the first part of the paper, the subgrid-scale model used is the Smagorinsky model with Van Driest damping near walls and a model constant $C_s = 0.1$. In the second part, the dynamic model of Germano et al. (1991) has been employed, with least squares averaging

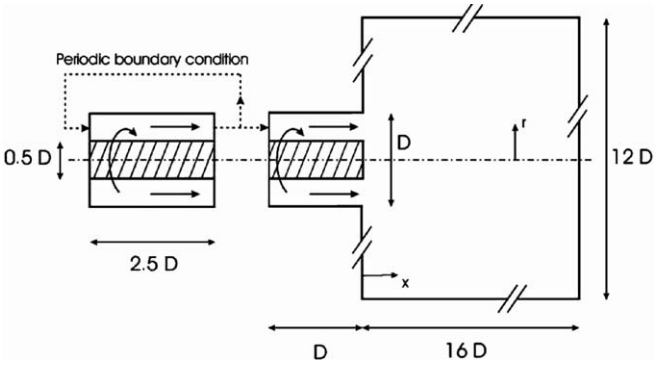

Fig. 1. Sketch of computational domain and boundary conditions for the swirl study.

and three-dimensional test filtering with twice the grid size. The eddy viscosity in the latter case is smoothed by temporal relaxation (Breuer and Rodi, 1994). In what follows, capital letters are used to indicate values averaged in time and circumferential direction while the superscript ϕ^{rms} designates the root mean square (RMS) of a quantity ϕ. Mean quantities were obtained by averaging in time over at least $100t_b$ with $t_b = R/U_b$ where U_b is the bulk velocity of the jet, further enhanced by averaging in azimuthal direction.

The inflow conditions are obtained by performing simultaneously a separate periodic LES of swirling flow in an annular pipe using body forces to impose swirl and flow rate as described in Pierce and Moin (1998b). This approach is illustrated in Fig. 1. No-slip boundary conditions are applied at the walls. The fluid to be entrained by the jet was introduced using a weak co-flow of 5% of the bulk velocity in the outlet plane $x/R = 0$ remote from the jet. Free-slip conditions are applied at the open lateral boundary which is placed far away from the region of interest (see Fig. 1). The entire modelling of boundary conditions has been validated in García-Villalba et al. (2004b). Further details are given in García-Villalba (2006).

3. Sensitivity to the level of swirl

An overview of the simulations performed is shown in Table 1. The Reynolds number of the flow based on the bulk velocity $U_b = 25.5$ m/s and the outer radius of the jet $R = 50$ mm is $Re = 81{,}500$. The swirl parameter is defined at the inflow plane $x/R = -2$ as

$$S = \left(\int_0^R \rho U_x U_\theta r^2 \,\mathrm{d}r\right) \Big/ \left(R \int_0^R \rho U_x^2 r \,\mathrm{d}r\right) \tag{1}$$

where U_x and U_θ are the mean axial and azimuthal velocities, respectively. The range covered by the simulations is very wide, including a simulation without swirl, Sim 1, another with a low level of swirl, Sim 2, and three simulations with a high level of swirl, Sim 4, 5, 6. There is also a simulation with an intermediate level of swirl, Sim 3. For orientation it should be recalled that for a round jet (i.e. not

Table 1
Overview of the simulations performed to investigate the impact of the swirl number

Simulation	1	2	3	4	5	6
Swirl number S	0	0.4	0.55	0.7	1	1.2
Line style	Solid (thin)	Dashed–dotted	Dashed–×	Dotted	Dashed	Solid (thick)

featuring a bluff body in the centre) recirculation is observed for $S \geqslant 0.6$ with S being measured at the outlet plane (Gupta et al., 1984).

Fig. 2 addresses the inflow conditions for the main simulation imposed at $x/R = -2$. It shows the mean axial and azimuthal velocity components resulting from imposing the desired swirl number in the precursor simulation. In fact, the mean azimuthal velocity increases almost proportional to S with little change in the shape of the profile. The mean axial velocity is almost unchanged in all cases.

3.1. General features of the flow

Fig. 3 shows the two-dimensional streamlines of the average flow in an axial plane from selected simulations in Table 1. As the jet is annular, the flow characteristics differ from those of a usual round jet. In the non-swirling case, Fig. 3(a1), a geometry-induced recirculation zone (GRZ) is formed due to the bluff-body effect of the cylindrical centre body. Its length is equal to the diameter of the center body which agrees well with data from the literature (Rehab et al., 1997). Fig. 3(b1) shows the case of low swirl, Sim 2. In this case, additional to the GRZ, a very thin central recirculation zone (CRZ) appears close to the axis. It extends up to about $x/R = 4$. For this level of swirl, no CRZ is expected in a round jet (Gupta et al., 1984), but in the present case the presence of the GRZ facilitates the formation of the CRZ. Increasing S leads to an increase in the size of the CRZ. For $S = 0.7$, Fig. 3(c1), the length of the CRZ is about $4R$, and its width is increased to $0.6R$, attained at $x/R = 2$. The GRZ is still present at this level of swirl but substantially reduced in size and strength. For $S = 1$, not shown here, the CRZ is longer reaching until $x/R = 8$ and attaining its maximum width of $0.8R$ at $x/R = 1.5$, i.e. further upstream compared to Sim 4. Finally, Fig. 3(d1) displays the case $S = 1.2$, in which the CRZ has reached $x/R = 0$, and the GRZ has been merged into the CRZ. The length of the CRZ is about $10R$ and the maximum width of $0.8R$ is attained at $x/R = 1$. Fig. 3 shows that with increasing swirl number the jet spreads further outwards in radial direction and the strength of the CRZ increases substantially. Let us finally address the slope of the streamlines in Fig. 3 remote from the jet, starting at $x/R = 0$ and $r > R$. Their shape is due to the co-flow boundary condition. Note, however, that the velocity at this location is only 5% of the jet axial velocity, so that the influence on the region of interest is negligible, as will be seen in Fig. 4. This was also verified by repeating the same simulation with different amounts of co-flow in García-Villalba (2006).

Due to the swirl of the jet the average streamlines are highly three-dimensional. So far, only the two-dimensional streamlines of the flow projected onto the x–r plane were addressed. To complete the picture the angle

$$\alpha = \text{arc tg}\left(\frac{U_\theta}{U_x}\right) \tag{2}$$

between the mean flow and the x-axis is displayed in a second set of graphs in Fig. 3 (in the non-swirling case $\alpha = 0$ so that the picture is dropped). These plots all exhibit a similar structure. For large radii, i.e. in the outer flow, $\alpha = 0$. At the outer border of the jet a steep increase is observed with a local maximum. For $S = 0.4$, the maximum occurs around $x/R = 1$ while for the cases with higher swirl the local maximum occurs further downstream at about $x/R = 2$. Inward from this zone a local minimum of α is observed which coincides with the interior of the jet and the maximum of U_x in the high-swirl cases (see Fig. 4(b1) and (c1)). Further towards the axis the flow angle increases again, now beyond 90° which corresponds to the boundary between forward and backward flow. The value of the local maximum in the outer part increases with the swirl number and this zone gets broader and straighter. It in fact

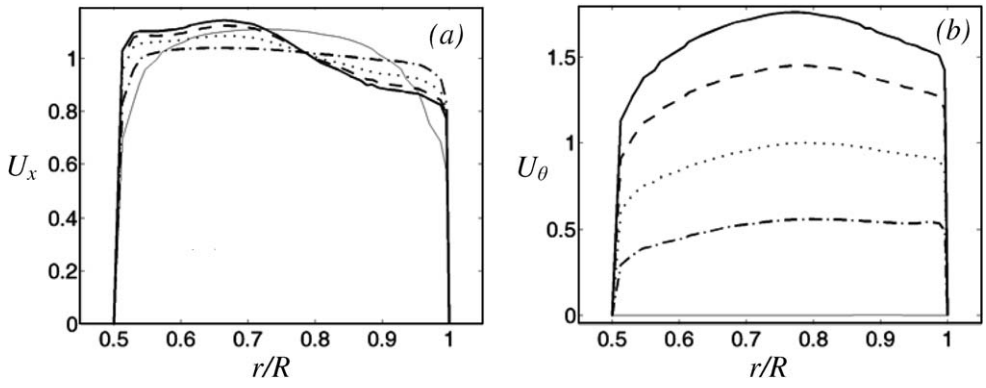

Fig. 2. Mean velocity deduced from the fluctuating inflow conditions imposed at $x/R = -2$ for different levels of swirl. (a) Mean axial velocity U_x as a function of the radial coordinate r/R and (b) mean tangential velocity U_θ. Line styles are defined in Table 1.

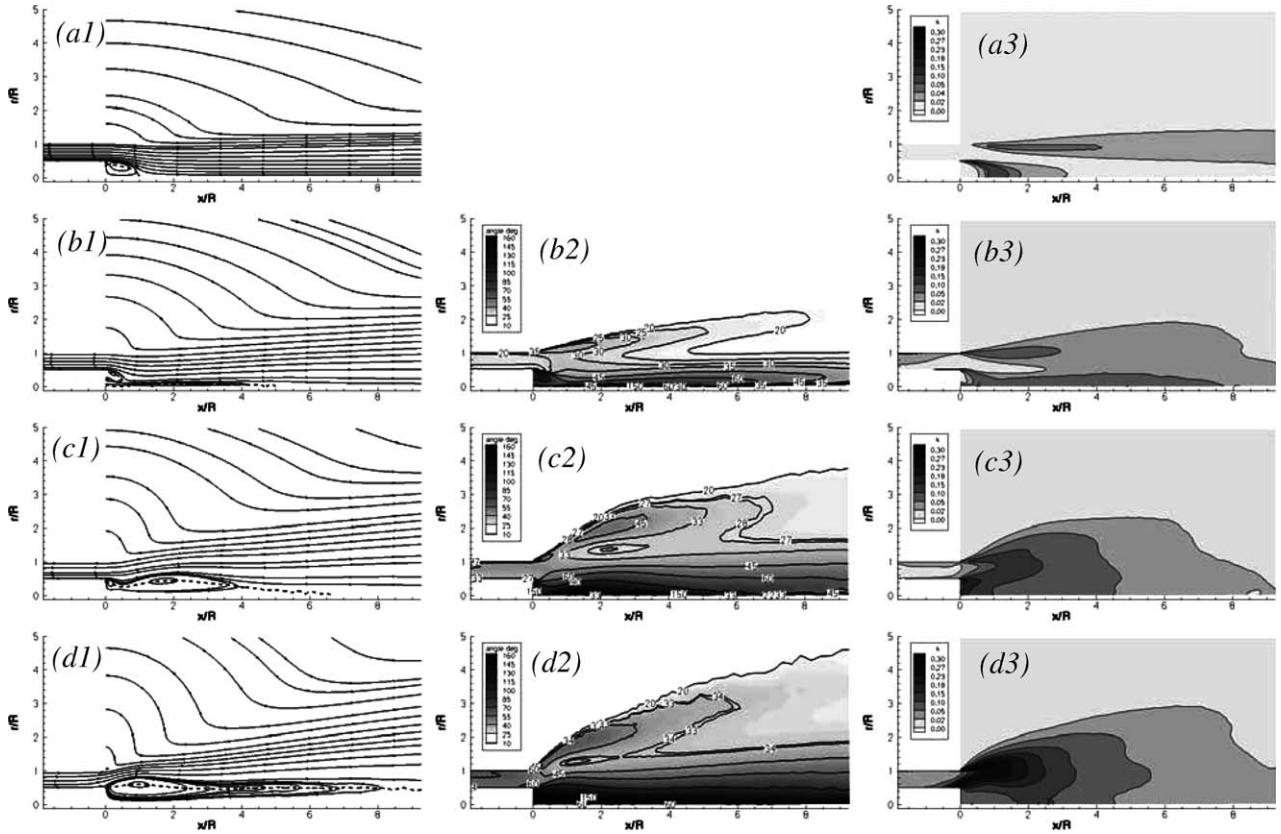

Fig. 3. Mean flow and fluctuations in the x–r-plane. Column 1: Streamlines of the average flow (solid lines, streamlines; dashed line, $U_x = 0$). Column 2: angle of the flow α, is defined in the text. Column 3: Fluctuating kinetic energy: (a) Sim 1. (α is not shown because it vanishes for $S = 0$), (b) Sim 2, (c) Sim 4 and (d) Sim 6.

identifies the outer border of the jet and its spreading even clearer than the x–r streamlines.

To conclude the general description of the flow, Fig. 3 displays grayscale contours of the fluctuating kinetic energy. The same scale has been used for all simulations to stress the fact that with increasing swirl the level of fluctuating kinetic energy increases dramatically. The maximum kinetic energy in the case $S = 0$ is about $k_{\max} = 0.05U_b^2$ while in case $S = 1.2$ it is about $k_{\max} = 0.3U_b^2$. For $S = 0$, the kinetic energy is concentrated in the recirculation zone (GRZ) and in the outer shear layer, Fig. 3(a3). The same happens for $S = 0.4$ but now the recirculation zone, which is the CRZ in this case, is substantially longer. With increasing swirl, the kinetic energy concentrates in the two shear layers and close to the jet outlet, $x/R < 2$. It also decays fast with axial direction, i.e. for $S = 1.2$ it decays from $k/U_b^2 \sim 0.3$ at $x/R = 0.5$ to $k/U_b^2 \sim 0.15$ at $x/R = 2$ and $k/U_b^2 \sim 0.05$ at $x/R = 4$. For this level of swirl, furthermore, a patch of kinetic energy extends into the inlet duct, Fig. 3(d3).

3.2. Mean and RMS velocity profiles

Experimental data were available only for one flow condition, equivalent to $S = 1.2$. In the graphs discussed below, experimental values obtained on two sides of the nominally symmetric jet are plotted with respect to their radial coordinate. This provides a qualitative impression of the uncertainty of these data. The agreement between the experiment and the present simulations is generally very good. Fig. 4 shows mean velocity and turbulent intensity profiles at three axial positions in the near flow field of the jet. Fig. 4(a1–4) shows profiles very close to the jet exit at $x/R = 0.2$. Here, the jet forms two complex three-dimensional shear layers, the inner one with the recirculation zone, and the outer one with the surrounding co-flow. At this position, $x/R = 0.2$, the inner one increases in thickness with S, reaching $0.5R$ for $S = 1.2$, while the outer one remains thin and is just displaced radially outwards with increasing S. The axial fluctuations in Fig. 4(a3) exhibit a peak in the region of the shear layer. The thicker the shear layer, the more pronounced and wider is the peak. The outer shear layer does not present these variations, but with increasing S, the velocity-difference is larger, and therefore the turbulence intensity is also larger. The velocity difference is generated by both axial and azimuthal velocity and hence complemented by Fig. 4(a2) showing mean tangential velocity profiles. Similar conclusions as for the axial fluctuations hold for the azimuthal ones in Fig. 4(a4).

A bit downstream at $x/R = 1$, Fig. 4(b1–4), some trends can be detected. The backflow in the inner region increases

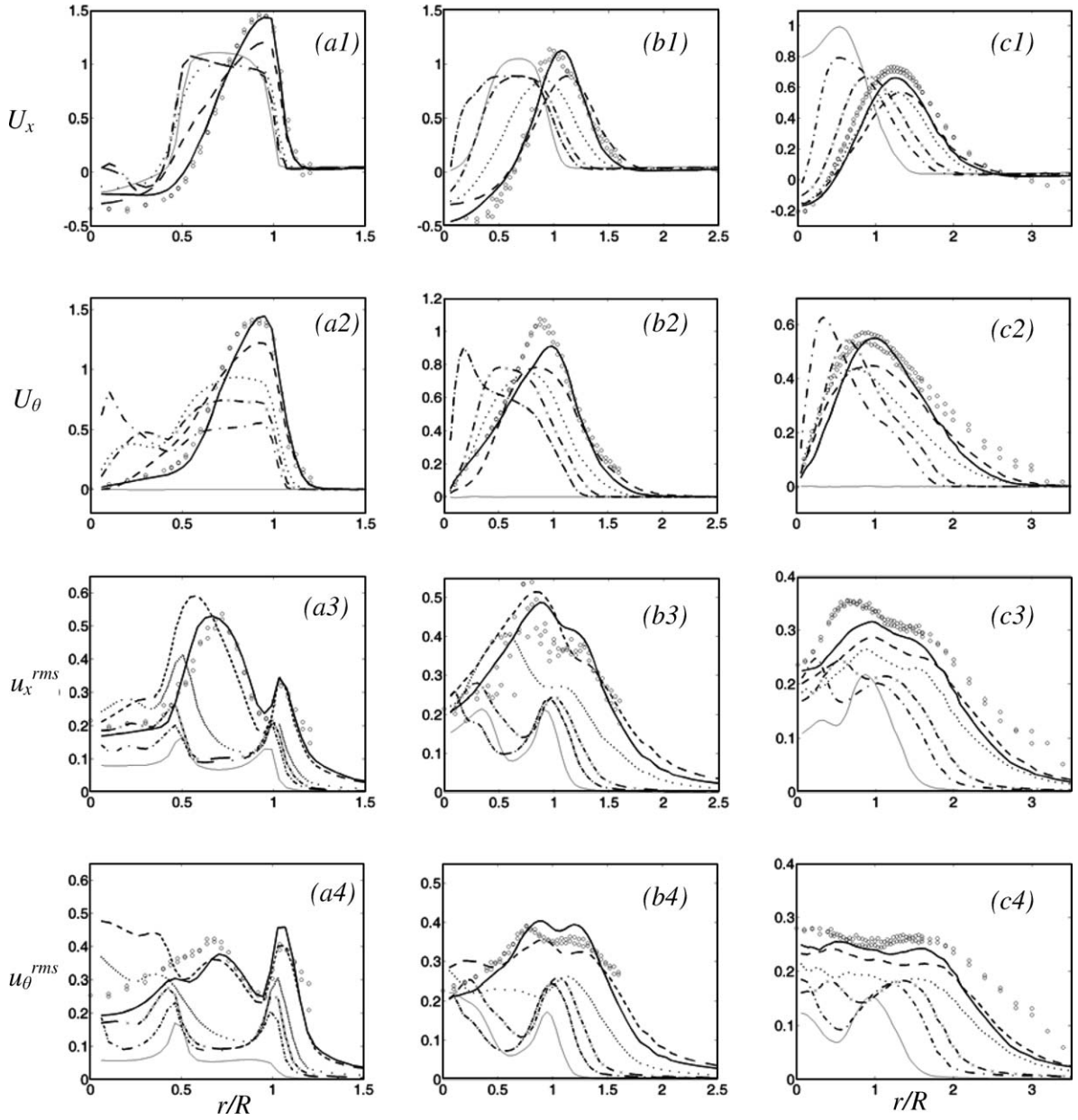

Fig. 4. Radial profiles of mean flow and corresponding RMS fluctuations: (a) $x/R = 0.2$, (b) $x/R = 1$ and (c) $x/R = 3$. Row 1: mean axial velocity component. Row 2: mean tangential velocity. Row 3: RMS of axial velocity. Row 4: RMS of tangential. The line styles are defined in Table 2. Symbols represent experimental data of Büchner and Petsch (2004). To enhance readability the range of the vertical axis has been adjusted individually.

with the level of swirl, Fig. 4(b1), and the width of the recirculation region as well. It is interesting to note that the maximum tangential velocity, Fig. 4(b2), is similar for all cases (except the non-swirling case) despite the difference of swirl at the inlet. The profiles of tangential velocity are displaced radially outwards with increasing swirl. Thus, although the maximum tangential velocity is similar for all cases, the angular momentum increases with increasing swirl. The profiles of axial and tangential fluctuations, Fig. 4(b3–4), show similar features as the corresponding graphs at $x/R = 0.2$. The level of turbulence increases with the swirl and the fluctuations concentrate in the regions of the shear layers. At $x/R = 1$, the shear layers are broader than further upstream and approach each other. For $S \geqslant 1$a single broad peak is observed for the fluctuations with a small local minimum (or a turning point for the axial fluctuations) reminiscent of the two individual layers.

Fig. 4(c1–4) shows the same profiles at $x/R = 3$. This position is located within the CRZ in the simulations with swirl. A qualitative difference between the simulations with $S \leqslant 0.55$ and the simulations with $S \geqslant 0.7$ is observed in all data. The spreading and decay rate is much lower in the former, Fig. 4(c1–2). The profiles of mean velocity and fluctuations in Sims 4–6 do not present substantial differences at this location. As soon as the swirl is high enough to produce a strong recirculation zone, a kind of saturation of the profiles is reached. The shape of the turbulent intensities is also the same, Fig. 4(c3) and (c4), with a slight increase of

intensity with S. At this position, the distinction between shear layers is not reflected by the profiles of the fluctuations. Only for the low swirl cases, it is still possible to distinguish the peaks due to the fact that these flows develop slower in space than the others.

3.3. Coherent structures

In García-Villalba et al. (2006) large scale coherent structures were identified and their evolution and interaction described for a high swirl number case, equivalent to Sim. 6. It was shown that two families of structures appear, which are best visible in Fig. 5(c). The outer, spiralling structure is located in the outer shear layer which can be identified in Fig. 4(a1). Here $\partial U_x/\partial r < 0$, and the iso-surface is coloured light. The darker one is located in the inner shear layer between the annular jet and the recirculating fluid where $\partial U_x/\partial r > 0$. In the cited reference it has been shown that these structures result from Kelvin–Helmholtz instabilities as they are perpendicular to the average streamlines. It is now interesting to study how these structures are modified when varying the swirl number. This is reported in Fig. 5. Due to lack of space, only one snapshot is included but further views and animations were produced upon which the following comments are based. In the literature on the subject the inner structure is usually called 'precessing vortex core' (PVC), (Gupta et al., 1984). In the case of low swirl, this feature is not expected. However, as in the present case a very thin CRZ is produced, a thin elongated structure can be seen in Fig. 5(a) for $S = 0.4$. Larger values of $p' = p - P < 0$ do not show any large scale structure in these data.

In the case of strong swirl both structures mentioned above are observed. For $S = 0.7$, a single inner and a single outer structure are present. Animations of the flow show that their rotation is in phase and very regular. Upon increasing S, Fig. 5(d) and (e), the irregularity of the flow grows in the sense that the PVC change in number during their evolution. For $S = 1.2$, up to three of them can coexist at certain instants. Furthermore, with increasing S, the inner structures enter the inlet duct, slightly for $S = 1$, and in a more pronounced way for $S = 1.2$. At the same time the PVC is displaced off the symmetry axis since the shear layers are shifted outwards as discussed above. As a consequence, the tangential fluctuations near the axis increase for $S = 0$ to $S = 1$ while decreasing for the larger value $S = 1.2$. The radial fluctuations behave similarly.

The outer structures consist of a long spiral for $S = 0.7$ and also become more irregular with increasing swirl. Another interesting feature is that the separation between the inner and the outer structures decreases with increasing S, to the point that in absence of colour it is difficult to distinguish them when $S = 1.2$. The reason for this behaviour is that the two shear layers, identified as the origins and locations of both types of structures, approach each other with increasing S, as seen in Fig. 4(a1).

The case $S = 0.55$ constitutes an intermediate situation between the two regimes of low and high swirl discussed so far. Here, structures are only generated in the inner shear layer, more precisely two of them, and none in the outer shear layer. These structures are located closer to the axis than the PVC for $S = 0.7$ to $S = 1.2$ and also start further downstream. They precess around the axis in a very regular manner. The fact that in this simulation only inner structures are observed suggests that the inner shear layer is more unstable than the outer one, although the thickness of the latter is substantially smaller (Fig. 4). This issue, as well as the synchronization between both types of structures, furthermore suggest that the structures in the outer layer are generated by the inner ones. With increasing swirl number, the scenario would then be the following. For low swirl, the CRZ is formed and no instability occurs. Further increasing the swirl, the inner shear layer becomes unstable so that the inner structures are formed. In this case the two shear layers are far from each other (Fig. 4(a1)) and the inner structures are relatively weak. Hence, their impact on the outer shear layer is small and not able to generate the large-scale instability there. With $S = 0.7$ and larger, the two layers approach further so that the inner structures generate the outer ones with a synchronized rotation of both.

Comparing the three cases $S = 0.7$, 1.0, 1.2 in Fig. 5 shows that the outer spiralling structures form an increasing angle with the plane $x = \text{const.}$ when the swirl increases. By close visual inspection a typical angle of 26°, 30° and 33° has been determined from such pictures for$S = 0.7$, 1.0, 1.2, respectively. It is now interesting to relate these values to the flow angle α displayed in Fig. 3. In the above discussion it was noted that the local minimum of α is located roughly in the interior of the main jet which in fact corresponds to the position where inner and outer shear layer touch. The corresponding inner-most level lines are $\alpha = 26°$ for $S = 0.7$ and $\alpha = 33°$ for $S = 1.2$, respectively, while the same plot for $S = 1.0$ (not shown here) yields $\alpha = 30°$ in this point. Hence, the angles of the coherent structures correspond very well to the local minima of the flow angle. This supports the observations in García-Villalba et al. (2006) where streamlines of the average flow were inserted into plots of the coherent structures to show that the latter are perpendicular to the average flow thus supporting their generation by a Kelvin–Helmholtz instability. The present way of investigating this issue is substantially less tedious and yields a more precise picture.

3.4. Spectra

Power spectra were computed from time signals, typically of length $120t_b$with $t_b = R/U_b$ using a windowed Fourier transform with overlapping segments of length about $30t_b$, averaging the spectra over the segments. Additional averaging was done using signals recorded at 12 different angular positions. Fig. 6 shows the power spectrum density (PSD) of axial velocity fluctuations at $x/R = 0.1$, $r/R = 0.7$, i.e. very close to the jet exit and in the region of the inner

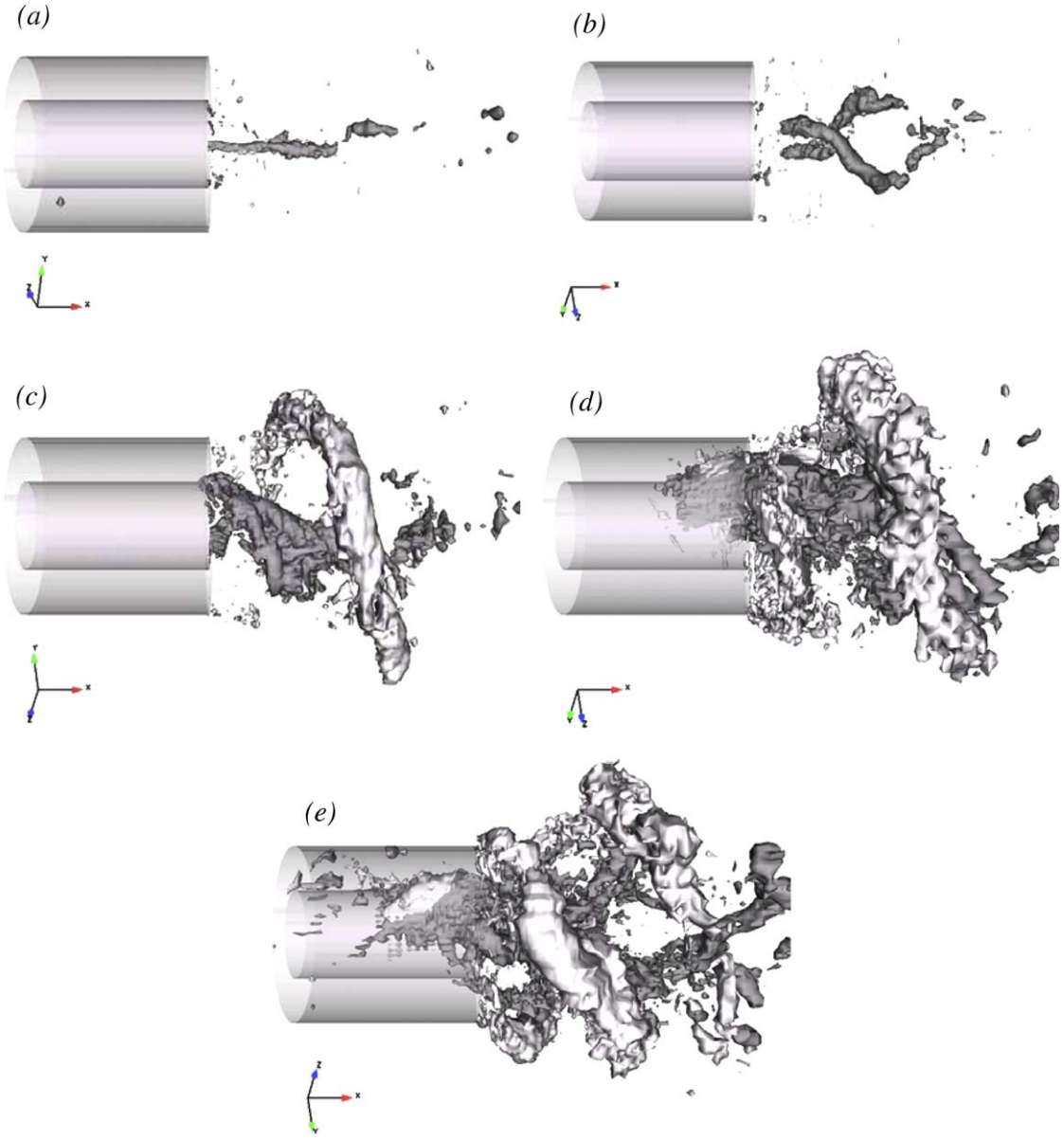

Fig. 5. Instantaneous coherent structures visualized using an iso-surface of the instantaneous pressure deviation $p' = p - P = -0.2$. (a) Sim 2, (b) Sim 3, (c) Sim 4, (d) Sim 5 and (e) Sim 6. The colour is computed according to the sign of the radial gradient of the mean axial velocity, dark $\partial U_x/\partial r > 0$, light $\partial U_x/\partial r < 0$.

shear layer for all cases. With low swirl the spectra do not show a pronounced peak. When the level of swirl is high, i.e. $S \geqslant 0.7$, a dominant peak and its higher harmonics appear in the spectrum. This peak reflects the precessing structures observed in Fig. 5(c–e) (García-Villalba et al., 2004a). Its frequency is almost constant with increasing swirl number, more precisely $f_{\text{peak}} = 0.24 U_b/R$ for $S = 0.7$ and $S = 1$ and $f_{\text{peak}} = 0.28 U_b/R$ for $S = 1.2$. This constancy is unexpected at first sight since the level of swirl is increased by about 70%. Even if the swirl is attenuated between $x/R = -2$ and $x/R = 0.2$ due to friction as can be appreciated by comparing Figs. 2(b) and 4(a2), the variation of swirl and hence circumferential velocity remains substantial between the three cases. The reason for the observed behaviour of f_{peak} is presented in Fig. 7. The shape of the velocity profiles at $x/R = 0.2$ changes substantially from $S = 0.7$ to $S = 1.2$, turning from a top-hat-like shape to a more triangular shape. As discussed above, the inner structures are generated by an instability of the inner shear layer. The center of this layer has been marked with a dot in Fig. 7 displaying the azimuthal velocity. Its location has been obtained by first adding vectorially U_x and U_θ, then visually determining the velocity values at both boundaries of the shear layer and choosing their mean value. It turns out that the center of this shear layer shifts outward with increasing S. At the same time the angular velocity at this center increases. While it is not possible to apply the theory of plane shear layers directly, as discussed above, it can be stated that qualitatively the increased swirl is located further outward in the annular

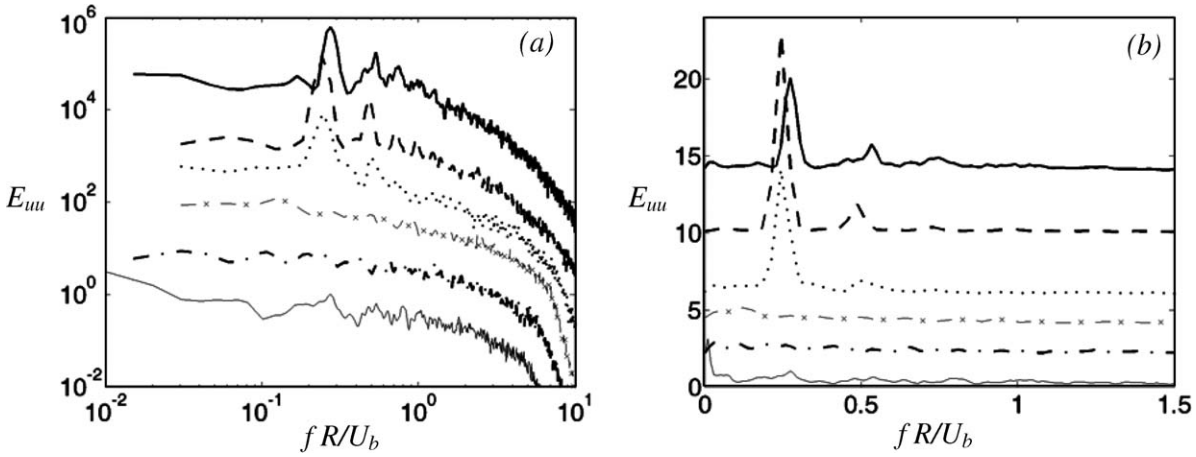

Fig. 6. PSD of axial velocity fluctuations at $x/R = 0.1$, $r/R = 0.7$. Arbitrary units are used in the vertical axis and the curves have been shifted vertically for readability: (a) Diagram with logarithmic axes and (b) the same diagram with linear axes. The line styles are defined in Table 1.

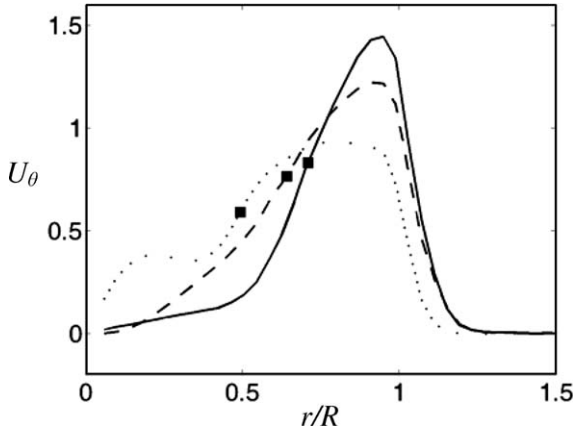

Fig. 7. Radial profiles of the mean tangential velocity at $x/R = 0.2$ for the cases $S = 0.7$, 1 and 1.2. Symbols identify the middle of the shear layer as detailed in the text.

jet so that the circumference to be covered is larger. With the same number of structures along the circumference the frequency can then remain constant. If only the azimuthal velocity at the location of the symbol would matter constant frequency would require the symbols to lie on a straight line going through the origin. This indeed is almost the case. Also for $S = 0.55$ precessing structures are observed in Fig. 5(b) and this should be reflected by the PSD. The monitoring point, however, selected *a priori* at $r/R = 0.7$ for all runs is not crossed by the structures in this case. They occur closer to the axis and further downstream as discussed above. As a consequence, no peak is observed in the PSD for $S = 0.55$ provided in Fig. 6.

4. Influence of a pilot jet

4.1. Configuration

In the second part of the paper, the effect of an additional inner jet is studied. The inflow part of this configuration differs from the one described in Fig. 1 while the rest of the computational domain is identical. Here, the precursor simulation for the main annular jet is replaced by a duct reaching to $x = -3.82R$ and bending radially outwards to $r = 2.18R$. Fig. 8 shows a zoom of the inflow geometry for this case. The flow is prescribed at the circumferential inflow boundary located at the beginning of the inlet duct. The flow comes in radially, having an azimuthal component. At this position, where in the experiment the swirl generating device is located, steady top-hat profiles for the radial and azimuthal velocity components are imposed in the simulations. The flow undergoes a rapid pseudo-transition as displayed in Fig. 8 so that the kinetic energy in the annular pipe corresponds to the level observed in a developed annular jet. The coherent structures downstream of the outlet are substantially more energetic than the ones in the pipe flow so that the levels of kinetic energy k in this figure were restricted to low values to make this transition visible. Provided that the swirl at the inflow station is appropriately adjusted, this model for the inflow reproduces the experimental profiles of mean flow as well as fluctuations in the main jet near the outlet very well, as displayed in Fig. 10 below. A detailed discussion of this approach and a comparison with the precursor simulation

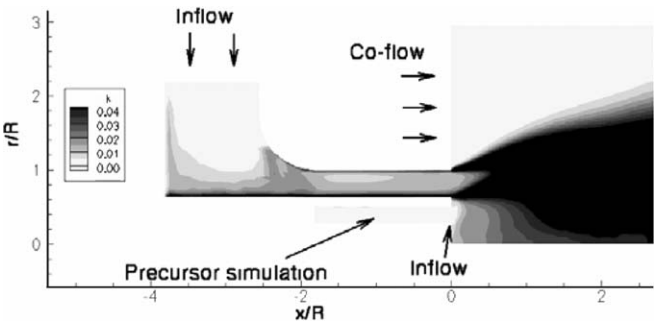

Fig. 8. Inflow conditions and geometry for the computations assembled in Table 2. Development of the fluctuating kinetic energy in the inlet duct for Sim 9. Only the lower levels of k are considered as discussed in the text.

technique of the previous section can be found in García-Villalba et al. (2004b).

In the experiment of Bender and Büchner (2005), a co-annular pilot jet was introduced. The swirl of this jet was co-rotating with the swirl of the main jet and created using an axial swirl generator. The blades of the swirl generator ended flush with the outlet plane at $x = 0$. Representing all of the 26 blades used in the experiment would have rendered the grid generation very complicated and would lead to low resolution of the channels between the blades. It was hence decided to model the pilot jet by a precursor simulation, similar to the inflow generation in the previous section. Since in the experiment the swirl generator ended at $x = 0$, these conditions were imposed at the same location. This is indicated in Fig. 8. In this configuration the inner and outer diameter of the pilot jet are $0.27D$ and $0.51D$, respectively, while the inner and outer diameter of the main jet are $0.63D$ and D, respectively. The flow conditions are very similar to the previous ones. The Reynolds number is $Re = 81{,}000$ based on the bulk velocity of the main jet alone, $U_b = 22.1$ m/s in the experiment, and on the outer radius of the main jet $R = 55$ mm. To allow comparison with the simulations of the previous section, the resulting swirl number in the main jet at $x = -2R$, has been determined. Its value is $S = 1.05$, almost exactly the same as for Sim 5. The different width of the main jet, however, precludes direct comparison with the above computations. The mass flux of the pilot jet is 10% of the total mass flux and the swirl number defined at $x/R = 0$ for the pilot jet alone is $S = 1$. The kinetic energy of the precursor for the pilot jet in Fig. 8 hence is by a factor of about 10 smaller as the kinetic energy in the main pipe.

Table 2
Overview of the simulations performed to investigate the influence of a pilot jet

Simulation	7	8	9	Experiment
Inner jet	No	Yes	Yes	Yes
Inner jet with swirl	–	No	Yes	Yes
Line style	Dotted	Dashed	Solid	O

The purpose of the simulations in this section is to clarify the impact of the inner jet on the stability of the entire flow. This is investigated by consideration of three cases which are summarized in Table 2: One simulation (Sim 7) without pilot jet, Sim 8 with a non-swirling pilot jet, and Sim 9 with swirling pilot jet. Note that experimental data are available only for the last case.

4.2. General features of the flow

The streamlines for the three cases investigated are displayed in Fig. 9. As already mentioned, the flow is expected

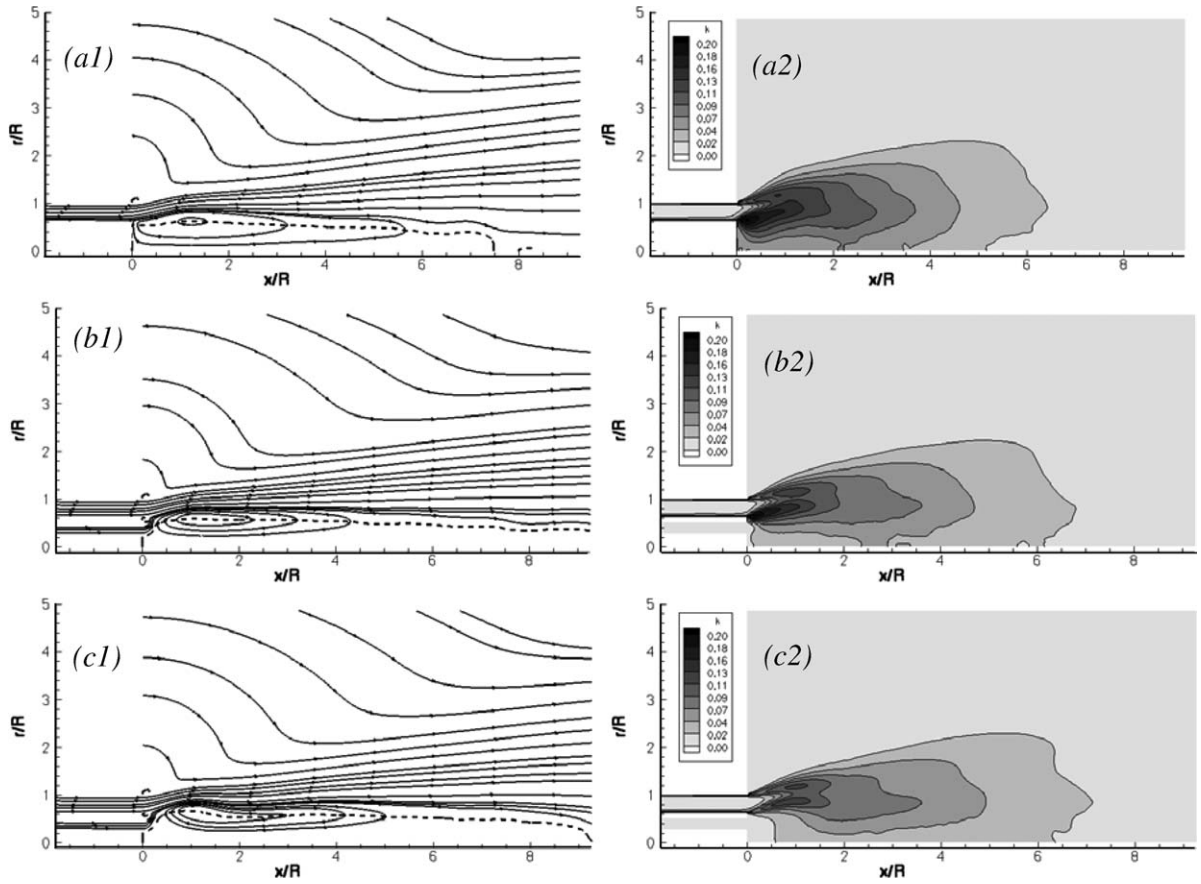

Fig. 9. Influence of the pilot jet on the mean flow. Column 1: Streamlines of the average flow. Column 2: Fluctuating kinetic energy. (a) Sim 7, (b) Sim 8 and (c) Sim 9.

to be similar to Sim 5 in the previous part due to the similar value of S. Hence, this falls into the high-swirl regime. The geometry is slightly different, however, and this introduces a difference in the flow. While in Sim 5 (not shown above) the GRZ and the CRZ are not merged yet, the GRZ and the CRZ are already merged in Sim 7, Fig. 9(a1), and the pattern is more similar to Sim 6 Fig. 3(d1). As before, a CRZ starting directly behind the cylindrical centre body occupies a long region near the symmetry axis. In Sim 8, featuring a non-swirling pilot jet, the resulting streamlines in Fig. 9(b1) are very similar to the ones without pilot jet. The streamlines issuing from the pilot duct just enter the inner shear layer without generating substantial alteration. In the case of the swirling pilot jet, Sim 9, the shape of the recirculation zone is slightly modified in the region of its maximum width. Here, the streamlines are shifted outward due to the higher total swirl which is also observed for the dotted line indicating the limit of the recirculation, where $U_x = 0$. Beyond $x/R = 3$ the flow is mostly unchanged.

The right column in Fig. 9 shows grayscale contours of fluctuating kinetic energy. As for the streamlines, the shape of the contour levels for the simulation without pilot jet, Fig. 9(a2), is close to the case with highest swirl of the previous configuration, Fig. 3(d3). The levels are slightly lower for Sim 7. As in Sim 6, the graphs show a concentration of kinetic energy close to the nozzle and a fast decay with axial direction. The data for k from all three simulations are very much alike. The differences between the three simulations occur in a small zone ($x/R < 2$) close to the jet outlet. In this region, Sim 7 features a higher level of kinetic energy than Sim 8 which in turn shows higher k than Sim 9, especially in the inner shear layer. For Sim 7 and Sim 8, the inner shear layer shows considerable values of k with $k_{\max} = 0.2U_b^2$ and $k_{\max} = 0.18U_b^2$, respectively, and is stronger than the outer one. The kinetic energy is lower for Sim 9 with $k_{\max} = 0.13U_b^2$ occuring in the inner shear layer. The latter also is narrower and located further outward, in compliance with the above discussion of streamlines. The turbulent kinetic energy immediately behind the center bluff body is substantially lower than in the case without pilot jet. The properties observed here originate from the vortical structures present in the respective cases which will be discussed below.

4.3. Mean and RMS velocity profiles

Fig. 10 shows radial profiles of mean velocity and the corresponding fluctuations at three axial positions in the near flow field of the jet for the three cases. Note also that only one of the simulations, Sim 9, corresponds to the experimental condition. The strength of the pilot jet can be appreciated by the mean axial and tangential velocity at $x/R = 0.1$ in Fig. 10(a1)and (a2). The deviation with respect to the experimental data in this range results from the model for the pilot jet. Its inflow condition is imposed at $x/R = 0$, while in the experiment the flow at this position can be influenced by the downstream flow. Downstream, at $x/R = 1$, the simulation overpredicts the backflow while the major part of the profile is very well captured, Fig. 10(b1). The mean tangential component also is in good agreement with the experiment, Fig. 10(b2). At this position the difference between the three cases is small for the mean profiles, with the tangential velocity profile displaced radially outwards for the simulation with swirling inner jet (Sim 9) compared to the simulation without inner jet (Sim 7). At $x/R = 3$, the agreement with the experiment is very good and the difference between the three cases is only marginal, Fig. 10(c1–4).

Fig. 10(a3–4)shows profiles of the RMS fluctuations of axial and tangential velocity profiles at $x/R = 0.1$. It can be appreciated that the region where the agreement is worst is precisely where the pilot jet is located, between $0.27R$ and $0.51R$. This is again due to the model for the pilot jet. The comparison of these turbulence intensity profiles for the three simulations shows higher values in the simulation without pilot jet, as expected from the contour plots of kinetic energy in Fig. 9. The disagreement is constrained to a small region close to the exit of the pilot jet. In Fig 10(b3–4) which shows profiles of the RMS fluctuations at $x/R = 1$, the fluctuations are already very close to the experimental data. At this location, it is still possible to appreciate a higher level of fluctuations in the simulation without inner jet, but the difference is smaller than at $x/R = 0.1$. In conclusion, Figs. 9 and 10 show that the influence of the pilot jet on the average flow and the second moments is only small.

4.4. Flow visualization and spectra

The instantaneous flow is now visualized in a similar way as in the previous section using iso-surfaces of pressure fluctuations, Fig. 11. Here, the pressure field was additionally smoothed in space by a two-fold application of a box filter of width twice the step size of the grid, in fact the test filter used in the dynamic model. Obviously, there are important differences between the three cases. Without pilot jet, Fig. 11(a), the structures have the characteristics described in the first part of the paper. They are very coherent, precess at a quasi-regular rate and persist over long time intervals. When the non-swirling pilot jet is introduced, Fig. 11(b), it is still possible to recognize similar structures as in the case without pilot jet. These are however substantially less coherent, much thinner, and do not reach downstream that far. In particular, the PVC are smaller and are more numerous along the circumference. In this case, four or five small PVC can co-exist at certain instants. Finally, the addition of swirl to the pilot jet has a dramatic impact on the flow, Fig. 11(c). The regularity is completely lost and the appearance of the structures is more random. Here, even the outer structures are affected and have almost vanished or, when they appear, exhibit only small coherence. The addition of near-axis swirl hence has a strong influence on the instantaneous flow character-

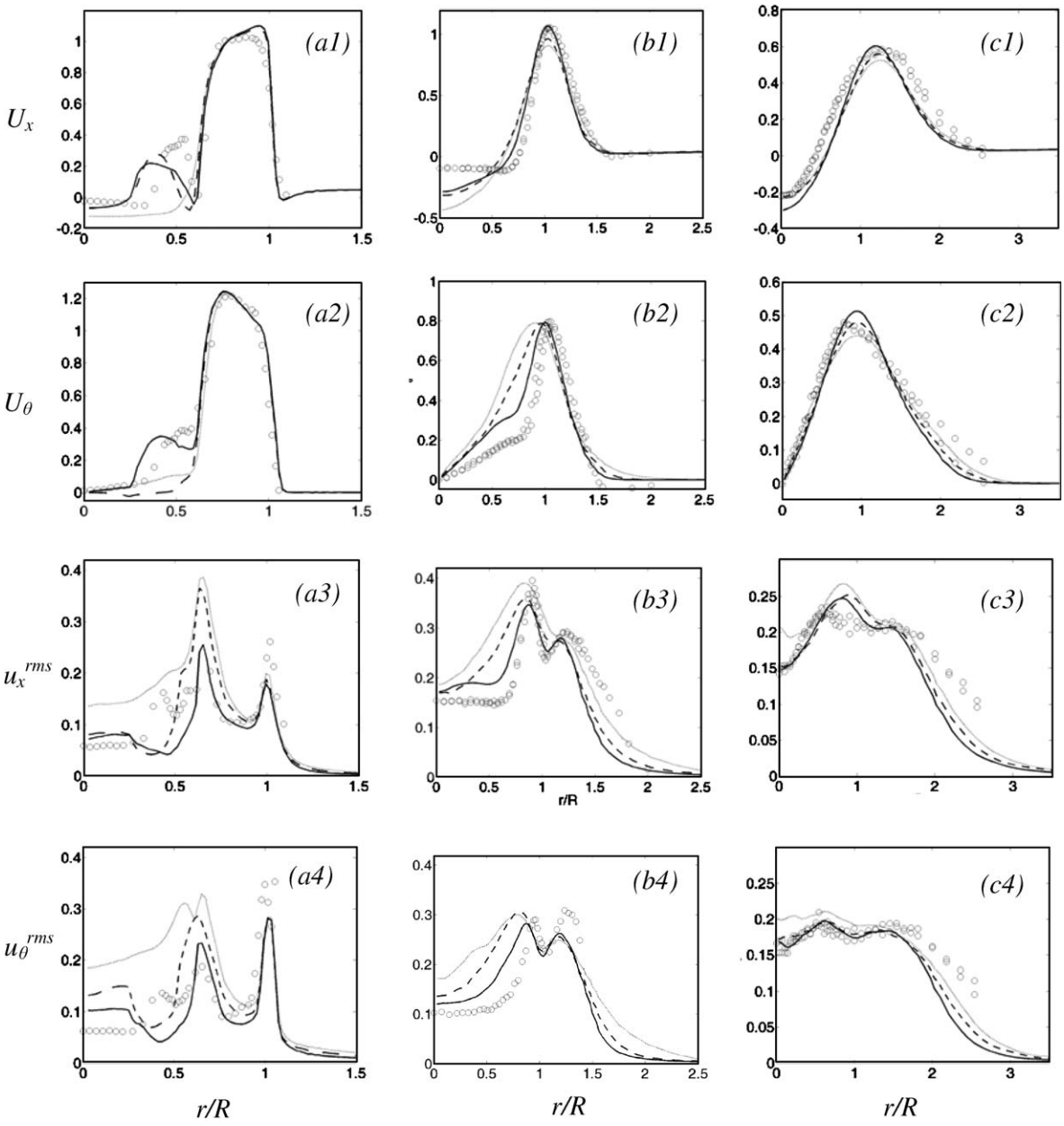

Fig. 10. Radial profiles of mean velocity and corresponding turbulent intensities: (a) $x/R = 0.1$, (b) $x/R = 1$ and (c) $x/R = 3$. Row 1: mean axial velocity component. Row 2: mean tangential velocity. Row 3: RMS of axial velocity. Row 4: RMS of tangential velocity. The line styles are defined in Table 2. Symbols represent experimental data of Bender and Büchner (2005). To enhance readability the range of the vertical axis has been adjusted individually.

istics. Recently, in a different context, the addition of near axis swirl has been proposed as a strategy to control vortex breakdown, Husain et al. (2003).

The previous analysis of the coherent structures is confirmed by analysing the PSD of the radial velocity fluctuations at two points close to the outlet at $x/R = 0.4$. Fig. 12(a) shows this data on the symmetry axis. Note that in spite of the difference in geometry with respect to the configuration studied in the previous section, the peak in the spectrum for Sim 7 also appears at a frequency $f_{\text{peak}} = 0.24 U_b/R$. The difference in geometry hence does not have much influence in the precessing rate of the structures. A pronounced peak can also be observed for Sim 8. The spectrum of Sim 9 also shows a peak but at substantially larger time scales. These are not well resolved with the length of the time segments employed for the computation of the spectra mentioned above. (Also note that no averaging over angular positions is possible for $r = 0$.) Repeating the analysis with longer segments shows that, indeed, a low frequency contribution with $f_{\text{peak}} \approx 0.025 U_b/R$ exists. This issue deserves further investigations, possibly relating it to work of Rehab et al. (1997) who observed low frequency oscillations with similar Strouhal number of the recirculation bubble created by an annular free jet without swirl.

Fig. 12(b) displays the PSD at $r/R = 0.6$, i.e. in the inner shear layer of the main jet. The spectrum of Sim 7 shows a

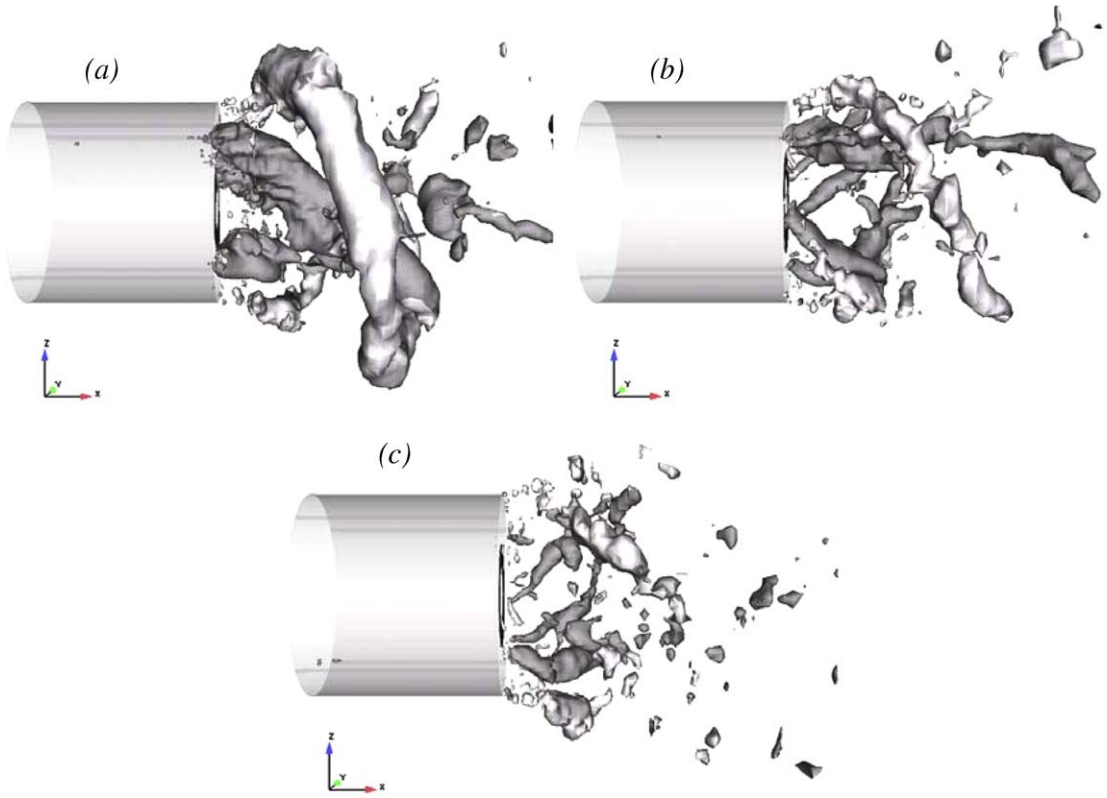

Fig. 11. Instantaneous coherent structures visualized using an iso-surface of the filtered instantaneous pressure deviation $p' = (p - P)_{\text{filt}} = -0.2$: (a) Sim 7, (b) Sim 8 and (c) Sim 9. Colour is given by the sign of the radial gradient of the mean axial velocity.

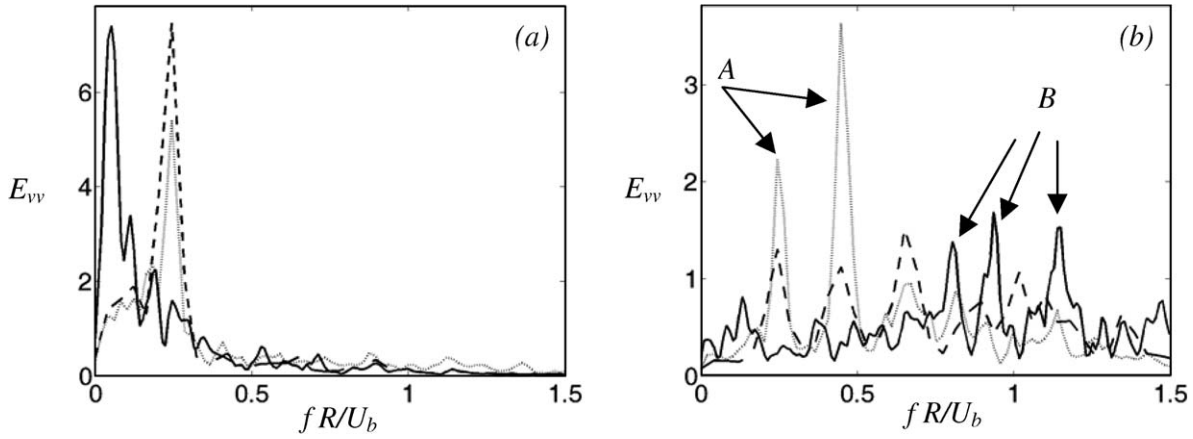

Fig. 12. PSD of radial velocity fluctuations at $x/R = 0.4$: (a) location on the symmetry axis, $r/R = 0$ and (b) location close to the inner diameter of the main jet, $r/R = 0.6$. The line styles are defined in Table 2.

pronounced first and second harmonic (both label A). The spectrum of Sim 8 also exhibits peaks at these frequencies, but their energy content is much smaller. Instead, more energy is displaced to the next harmonic, which shows that the PVC are more irregular in this case. For Sim 9 the energy is contained in substantially higher frequencies (the most dominant ones with label B) and much less in low-frequency modes. The analysis of this section hence explains the different levels of fluctuating kinetic energy encountered close to the nozzle in Fig. 9: the strong coherent structures observed in Sim 7 are destroyed by the addition of a non-swirling and even more of a swirling pilot jet.

5. Conclusions

The computations performed for an annular jet show dominating spiralling structures in the two shear layers present in this flow. Visualizations by iso-surfaces of pressure fluctuations coloured with the radial gradient of the mean axial velocity lend themselves to easy interpretation.

With increasing swirl number and S beyond 0.7, based on the definition employed here, their shape becomes more complex but the precessing frequency remains almost constant over a wide range. When a pilot jet is introduced close to the axis the average flow is only little affected while the fluctuations show moderate differences near the outlet and close to the inner shear layer. Visualizations and spectra however demonstrate that although axial and angular momentum of this jet are small, it has a dramatic effect on the instantaneous vortex structures. This is an important result for the consideration of mixing efficiency in this type of flow. Based on the data presented here more analyses of the flow field will be performed in the future. It would also be interesting to further modify the parameters of the pilot jet and, e.g., investigate the consequences of counter-rotating swirl.

Acknowledgements

This research is supported by the German Research Foundation through the collaborative research center SFB 606 'Unsteady Combustion' (www.sfb606.uni-karlsruhe.de). The references of the authors can be found on this website. The calculations were performed on the IBM Regatta of the Computing Center of Garching and on the VPP5000 of the Forschungszentrum Karlsruhe. The authors thank Prof. Wolfgang Rodi for stimulating discussions on the subject and Dr. H. Büchner and Mr. O. Petsch for providing the experimental data.

References

Bender, C., Büchner, H., 2005. Noise emissions from a premixed swirl combustor. In: Proc.12th Int. Congress on Sound and Vibration. Lisbon, Portugal.

Breuer, M., Rodi, W., 1994. Large eddy simulation of turbulent flow through a straight square duct and a 180° bend. In: Voke, P.R., Kleiser, R., Chollet, J.P. (Eds.), Fluid Mechanics and its Applications, vol. 26. Kluwer Academic.

Breuer, M., Rodi, W., 1996. Large eddy simulation of complex turbulent flows of practical interest. In: Hirschel, E. (Ed.), Flow Simulation with High Performance Computers II, Notes on Numerical Fluid Mechanics, vol. 52. Vieweg, Braunschweig, Germany, pp. 258–274.

Büchner, H., Petsch, O., 2004. Experimental investigations of instabilities in turbulent premixed flames. In: Proc. 1st Int. Workshop on Unsteady Combustion. Karlsruhe, Germany.

García-Villalba, M., 2006. Large eddy simulation of turbulent swirling jets. Ph.D. thesis, University of Karlsruhe.

García-Villalba, M., Fröhlich, J., Rodi, W., 2004a. Unsteady phenomena in an unconfined annular swirling jet. In: Andersson, H.I., Krogstad, P.Å. (Eds.) Advances in Turbulence X, pp. 515–518. CIMNE, Barcelona, Spain.

García-Villalba, M., Fröhlich, J., Rodi, W., 2004b. On inflow boundary conditions for large eddy simulation of turbulent swirling jets. In: Gutkowski, W., Kowalewski, T.A. (Eds.), Proc. of XXI International Congress of Theoretical and Applied Mechanics, 15.-21.8.2004, Warsaw, Poland, CD-ROM, IPPT PAN, ISBN 83-89687-01-1.

García-Villalba, M., Fröhlich, J., Rodi, W., 2006. Identification and analysis of coherent structures in the near field of a turbulent unconfined annular swirling jet using large eddy simulation. Phys. Fluids. 18, 055103.

Germano, M., Piomelli, U., Moin, P., Cabot, W., 1991. A dynamic subgrid-scale eddy viscosity model. Phys. Fluids A 3, 1760–1765.

Gupta, A.K., Lilley, D.G., Syred, N., 1984. Swirl Flows. Abacus Press, Kent, USA.

Hinterberger, C., 2004. Dreidimensionale und tiefengemittelte Large-Eddy-Simulation von Flach-wasserströmungen. Ph.D. thesis, University of Karlsruhe.

Hillemanns, R., 1988. Das Strömungs und Reaktionsfeld sowie Stabilisierungseigenschaften von Drallflamen unter dem Einfluss der inneren Rezirkulationszone. Ph.D. thesis, University of Karlsruhe.

Husain, H.S., Shtern, V., Hussain, F., 2003. Control of vortex breakdown by addition of near-axis swirl. Phys. Fluids 15 (2), 271–279.

Jakirlić, S., Hanjalić, K., Tropea, C., 2002. Modeling rotating and swirling turbulent flows: a perpetual challenge. AIAA J. 40 (10), 1984–1996.

Lu, X., Wang, S., Sung, H.-G., Hsieh, S.-Y., Yang, V., 2005. Large eddy simulations of turbulent swirling flows injected into a dump chamber. J. Fluid Mech. 527, 171–195.

Merkle, K., Haessler, H., Büchner, H., Zarzalis, N., 2002. Effect of Co- and counter-swirl on the isothermal flow- and mixture- field of an airblast atomizer nozzle. In: Rodi, W., Fueyo, N. (Eds.), Engineering Turbulence Modelling and Experiments, vol. 5. Elsevier, pp. 535–544.

Pierce, C.D., Moin, P., 1998a. Large eddy simulation of a confined coaxial jet with swirl and heat release. AIAA paper no. 98-2892.

Pierce, C.D., Moin, P., 1998b. Method for generating equilibrium swirling inflow conditions. AIAA J. 36 (7), 1325–1327.

Rehab, H., Villermaux, E., Hopfinger, E.J., 1997. Flow regimes of large-velocity-ratio coaxial jets. J. Fluid Mech. 345, 357–381.

Wang, P., Bai, X.S., Wessman, M., Klingmann, J., 2004. Large eddy simulation and experimental studies of a confined turbulent swirling flow. Phys. Fluids 16 (9), 3306–3324.

Wegner, B., Kempf, A., Schneider, C., Sadiki, A., Dreizler, A., Janicka, J., 2004. Large eddy simulation of combustion processes under gas turbine conditions. Prog. Comp. Fluid Dyn. 4, 257–263.